npj | climate and atmospheric science

www.nature.com/npjclimatsci

ARTICLE OPEN

Check for updates

An empirical study of the influences of gustiness on vertical mixing at the air-sea boundary

Meng Lyu[1]✉, Henry Potter[1], David G. Ortiz-Suslow[2], Qing Wang[2] and Xiaoqi Wang[1]✉

The exchange of momentum across the air-sea interface is a key driver of the earth system and its accurate parameterization is essential for precise weather and climate forecasting. However, our understanding of gustiness as an independent factor that can contribute to the momentum flux is limited. Using data collected from the R/P *FLIP*, as part of the Couple Air-Sea Processes and Electromagnetic ducting Research (CASPER) experiment, we explored the mechanisms by which gustiness contributes to the total interfacial momentum flux. We investigate how gustiness affects both the temporal and spatial (vertical) variance of turbulence in the atmospheric surface layer and show that high gustiness was associated with strong anisotropic turbulence at each measurement height. This was found to increase vertical wind fluctuations and inject additional momentum across the air-sea interface at lower wind speeds. Increased gustiness was also associated with the breakdown of the constant flux layer, which is generally assumed to exist over the ocean. This study has implications for both momentum flux parameterization and the use of similarity theory to model the flux-gradient relationship in the gusty atmospheric surface layer, thereby influencing the forecasting of climate and weather.

npj Climate and Atmospheric Science (2024)7:39 ; https://doi.org/10.1038/s41612-024-00577-6

INTRODUCTION

The exchange of turbulent momentum across the air-sea interface is a critical component of the earth system. Accurate parameterization of the momentum flux is key to precise climate and weather simulations, wave growth and breaking[1,2], currents[3], ocean mixing[4–6], and aerosol production[7]. The wind stress, $|\overline{\tau}|$, the vertical transport of horizontal momentum, is given by:

$$|\overline{\tau}| = \rho\left|\left[\left(-\overline{u'w'}\right)\vec{i} + \left(-\overline{v'w'}\right)\vec{j}\right]\right| \quad (1)$$

Here, u, v, w, are wind velocities in the along, cross, and vertical directions, respectively, primes denote fluctuating components, overbar is temporal average (O ~ 30 min), $\vec{i}, \vec{j}$ are unit vectors along and perpendicular to the mean wind direction, and ρ is air density. The friction velocity is defined as:

$$U_* \equiv \frac{\sqrt{|\tau|}}{\rho} \quad (2)$$

The momentum flux can be regarded as the square of friction velocity. Given a stationary and homogeneous surface layer with constant flux ($\frac{\partial \tau}{\partial z} \approx 0$), Monin–Obukhov similarity theory (MOST) predicts the relationship between the interfacial momentum flux and vertical mean wind gradient[8],

$$\frac{\partial U}{\partial z}\frac{zk}{U_*} = \phi(\varsigma), \quad (3)$$

where U is the mean wind speed, k is the von Kármán constant, z is height, and $\phi(\varsigma)$ is the dimensionless shear function which varies with stability $\varsigma = z/L$, the ratio of z with the Obukhov length[8]:

$$L = -\frac{U_*^3}{k\left(\frac{g}{T_0}\right)\left(\frac{q}{C_t\rho}\right)}. \quad (4)$$

Here, T_0 is surface temperature, g is acceleration due to gravity, q is kinematic heat flux, and C_t is specific heat. L is equal to zero for neutral stratification, is positive for stable conditions, and negative for unstable conditions. The value of L may vary from -∞ to ∞ with extremes of value corresponding to the limits of the heat flux approaching zero from the positive (unstable) or negative (stable) sides. Higher ς means stronger stability. According to the constant flux layer theory, U_* does not vary with height[9,10]. This is a key assumption when using point-based field measurements to estimate the momentum flux which are then used to develop bulk parameterization algorithms, e.g., COARE[11], that provide the physics for boundary layer schemes in atmosphere, ocean, and coupled models. Many studies have shown that U_* principally increases with wind speed[12–14] but many secondary factors also alter the momentum flux. These include wave age[2,15], swell[14,16,17], and surface currents[3]. However, the impact of gustiness on momentum fluxes is poorly understood.

The World Meteorological Organization quantifies gustiness using the gust decay time and the time interval between gusts and lulls, which reflect the spatial or temporal heterogeneity of the wind. Spatial and temporal gustiness, as two interconnected aspects of the same phenomenon, jointly quantify the intensity of small-scale air movement within the convective boundary layer, which cannot be adequately captured by the average wind speed alone. Some numerical models incorporate spatial gustiness by calculating the sum of squared u' and v' values for all points within a sub-grid[18]. Temporal gustiness refers to the temporal variability of the wind speed and direction within a period, which is commonly attributed to the presence of large-scale eddies within the convective boundary layer[19]. These gusts occur within a time range of one to ten minutes. Gustiness has been linked to precipitation and cloudiness[18,20] and shown to impact heat transport by influencing the convective system leading to changes in surface fluxes[21,22]. Consequently, by incorporating gustiness

[1]Department of Oceanography, Texas AM University, College Station, TX, USA. [2]Department of Meteorology, Naval Postgraduate School, Monterey, CA, USA.
✉email: meng@tamu.edu; cinky77@tamu.edu

into momentum flux parameterizations, climate models can reduce precipitation and evaporation bias particularly in the tropical oceans[23]. Gustiness also impacts macroscopic atmosphere boundary layer dynamics by altering the vertical profiles of kinetic energy and friction velocity over hundreds of meters[24]. Additionally, several experiments have shown that momentum flux is enhanced by gustiness[25,26]. In our recent work[27], we uncovered a connection between gusts and swell, highlighting their close relationship with the developmental stage of waves. This connection arises from the enhanced roughness of the sea surface associated with higher levels of gustiness, indicating a more robust air-sea coupling process. In this research, we modify the gustiness parameter in our previous research, G_0, by removing the covariance term, because it is negligible (see Eq. (6) in ref. [28]). Consequently, the influences of wind direction are adequately represented by *std*(*v*′), resulting in G being a vector following the convention of Eq. (1).

$$\vec{G} = \frac{\sigma_u}{U_{10N}}\hat{i} + \frac{\sigma_v}{U_{10N}}\hat{j}, \tag{5}$$

where σ_u, σ_v is the standard deviation of velocity [*u*,*v*]. To define the gustiness index G_0, the magnitude is taken:

$$\begin{aligned} G_0 &= \left|\vec{G}\right|, \\ G_0 &= \sqrt{\frac{\sigma_u^2+\sigma_v^2}{U_{10N}^2}}, \\ G_0 &= \sqrt{\sigma_u^2+\sigma_v^2}/U_{10N}, \end{aligned} \tag{6}$$

which reduces to $G_0 = \sigma_u/U_{10N}$, used in Babanin and Makin[25], in the case of $v = 0$ or when the crosswind component is neglected.

Despite previous studies showing that gustiness is a critical component of the earth system, it is often overlooked in climate and wave models, likely because its importance is underestimated and the mechanisms underlying its impact on momentum flux remain unclear. The primary objective of our study is to investigate and elucidate this underlying mechanism. By addressing this matter, we can enhance the accuracy of climate and weather prediction models, leading to improved responses to extreme weather events, wherein gustiness is likely to play a crucial role. Specifically, we will show how gusts contribute to momentum flux by transferring more energy from low-frequency wind flow into the vertical components of wind speed. The paper is laid out as follows: Results are introduced in Section "Results", Section "Discussion" is Discussion, Data and Method is introduced in Section "Method".

RESULTS

Environmental conditions during CASPER

The Couple Air-sea Processes and Electromagnetic Ducting Research (CASPER) experiment was designed to explore the marine atmospheric boundary layer and its coupling with the ocean surface with any eye to improve understanding of electromagnetic and electro-optical radiation propagation[27,29]. As part of CASPER, data were collected from the Floating Instrument Platform (*R/P FLIP*), in the Southern California Bight from September 22nd to October 25th, 2017. *FLIP*, in Fig. 1a, is a 108 m platform specially designed to minimize its response to surface waves, making it a stable ocean-going platform, ideal for air-sea flux studies. During the campaign, the wind was largely driven by the diurnal sea breeze oscillation, and varied between easterly wind before local noon and westerlies after local noon.

In our experiment, only data of wind direction from −90 to 90 degrees are used as shown in Fig. 2a. All cases are categorized as four different gusty conditions as shown in Fig. 2b. These are very low gusty ($G_0 < 0.12$), low gusty ($0.12 \le G_0 < 0.165$), high gusty ($0.165 \le G_0 < 0.21$), and very high gusty ($G_0 \ge 0.21$). Together we refer to the former two regimes ($G_0 < 0.165$) as non-gusty conditions and the latter two regimes ($G_0 \le 0.165$) as gusty conditions. We did not find any previously used classification methods due to the novelty of this work. Each of these four regimes occupies about 25% of the total data. We also experimented with different percentiles in classification (not shown), but the results remained consistent.

In Fig. 3, we present a plot depicting the wind speed and gustiness at the station. Wind speeds typically range of 3–6 m s^{-1}, however, from October 19 to October 21 a cold front passed through, and the wind speed reached a maximum of 14 m s^{-1}. Prior to the arrival of the cold front, a high gustiness event occurred. At other times, higher gustiness is associated with lower atmospheric stability during the diurnal sea-land breeze cycle. Gustiness in Fig. 3 is color-coded based on the stability parameter, $\varsigma = z/L$, calculated using Eq. (4), where *L* is derived from the data collected at 12.38 m due to its proximity to 10 m and $z = 12.38$ m. Blue indicates unstable ($\varsigma < -1$) atmospheric conditions, and red

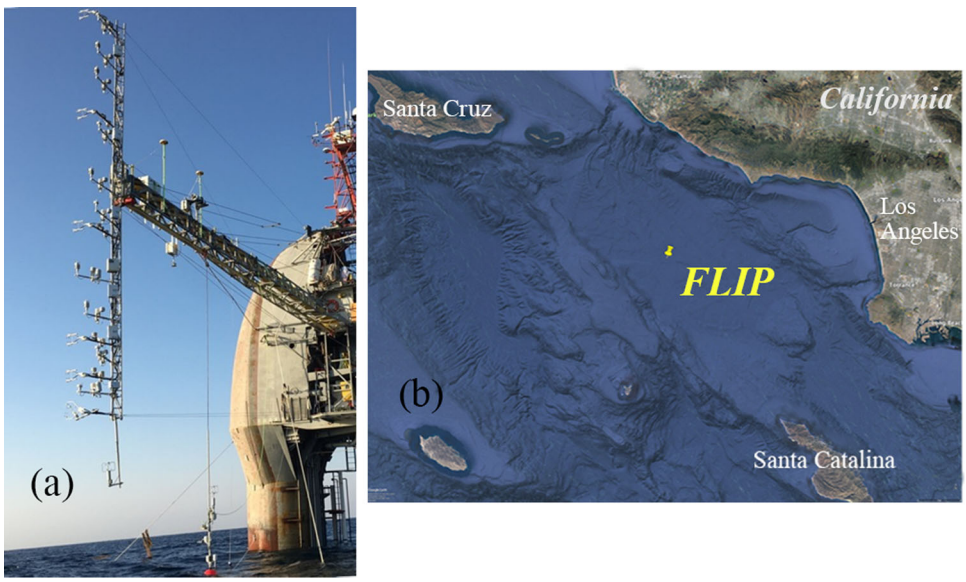

Fig. 1 Overview of the observation platform. a Snapshot of the Floating Instruments Platform[29]. **b** *FLIP*'s location during the CASPER campaign in the Southern California Bight.

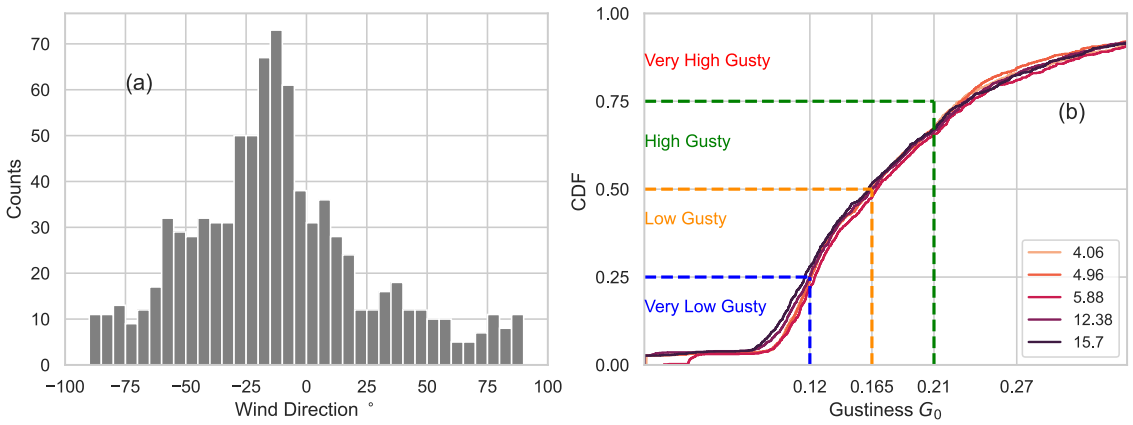

Fig. 2 Wind direction distribution and definition four gusty conditions. a Histogram of the wind direction. 0 degree marks the direction of the FLIP's mean heading with respect to the true north (290°). **b** Cumulative distribution function (CDF) of gustiness at different heights. The blue, orange, green vertical lines mark the lines of $G_0 = 0.12$, 0.165, 0.21.

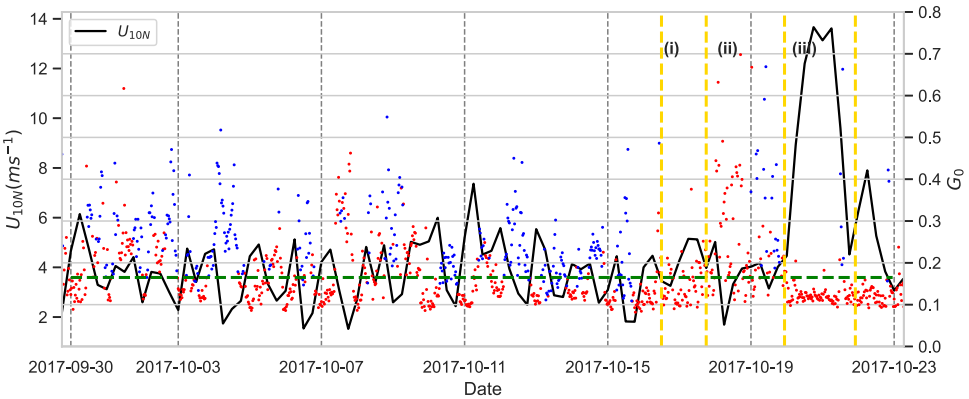

Fig. 3 Times series of averaged wind speed (U_{10N}, black line) and gustiness (dots) calculated from measurements at 12.38 m. The dots represent gustiness, with red indicating stable and neutral atmospheric conditions and blue indicating unstable atmospheric conditions. The green dashed line marks the $G_0 = 0.165$ above which conditions are classified as gusty. The wind speed and gustiness are averaged over six hours for simplicity. (i) & (iii) represent selected non-gusty periods and (ii) represents the selected gusty period addressed in the text.

represents both neutral ($-1 < \varsigma < 1$) and stable conditions ($\varsigma > 1$)[11]. A plot showing gustiness as a function of the stability (not included) did not exhibit any discernible relationship. This means gustiness here must be attributed to other factors, such as precipitation, cloudiness, and larger-scale atmospheric flow, which are known to impact gustiness. In Fig. 3, (i), (ii), and (iii) mark three specific periods of interest. During the approach of the cold front, the station experienced a period of low gustiness (i), followed by a period of high gustiness (ii). Upon the arrival of the cold front (iii), the wind speed reached its maximum and became less gusty. These three periods will be further discussed in Section "Discussion".

Atmospheric boundary layer structure under different gusty conditions

Figure 4a shows the vertical structure of wind speed under different gusty conditions, delineated by G_0. The wind is normalized by U_{10N} calculated from 12.38 m. We only select wind speeds above 3 m s^{-1} to show the vertical structure, thus highlighting cases with shear dominance. As gustiness increases, the wind speed gradient, $\partial u/\partial z$, decreases. This is likely attributed to the enhanced vertical mixing by gustiness, determined by Petersen et al. [30] who found wind speed profiles similar to those in Fig. 4. However, in their work, these changes were mainly attributed to the heat flux or thermal properties, furthermore, they lacked high-frequency data to support their conclusions. Figure 4b is a plot of G_0 as a function of U_{10N}. It shows that as the wind speed increases, the variability and intensity in gustiness decreases. The red line is the inverse linear regression fit between G_{10N} and U_{10N}. As predicted from Eq. (6), gustiness decreases as wind speed increases.

In Fig. 5 we present $std(u')/U_{10N}$ and $std(w')/U_{10N}$ profiles. Figure 5a shows that the standard deviation of the horizontal wind fluctuation remains constant with height. A similar pattern is also observed for $std(v)$ profiles (not shown). This indicates that the horizontal components of wind speed do not exhibit significant variations with height, and gustiness remains relatively constant within the lower marine atmospheric boundary layer. In Fig. 3b, there is a noticeable increase in $std(w')$ under higher gustiness. Concurrently, the profile of w' has a steeper slope under elevated gustiness, indicating a strengthening of vertical mixing. When wind speeds are low, high gustiness is typically caused by factors such as shifts in wind flow, atmospheric stability, and precipitation. The greater vertical gradient of $std(w')$ under gusty conditions signifies the enhanced eddy viscosity, which should be further related to the vertical mixing and energy dissipation at the air-sea interface, as w' approaches zero at the surface. Together, Fig. 5a, b, show gustiness allows for the presence of more energetic eddies that can be observed by the anemometer. This finding is relatively groundbreaking since gustiness is never found to be related to the vertical mixing at the air-sea boundary layer which further contributes to the momentum flux. In previous studies, no matter whether the boundary layer is experiencing high or low

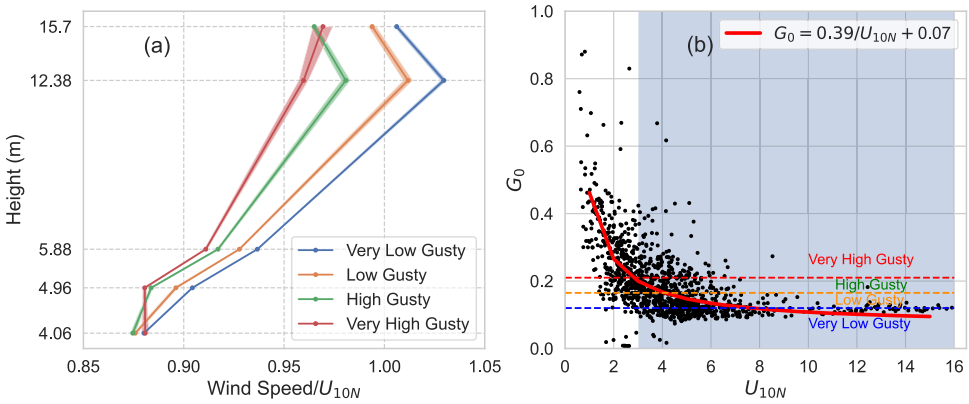

Fig. 4 Normalized wind speed profiles and the relationship between G_0 and U_{10N}. a Averaged wind speed profiles normalized by U_{10N} under different gusty conditions. Very low gusty condition (blue):$G_0 < 0.12$, low gusty condition (orange): $0.12 \le G_0 < 0.165$, high gusty condition (green): $0.165 \le G_0 < 0.21$, very high gusty condition (red): $G_0 \ge 0.21$. The shaded area marks the standard error of the mean. **b** Scatter plot of G_0 vs U_{10N}. Shaded area ($U_{10N} > 3$) marks the points used to plot wind profiles in subplot (**a**).

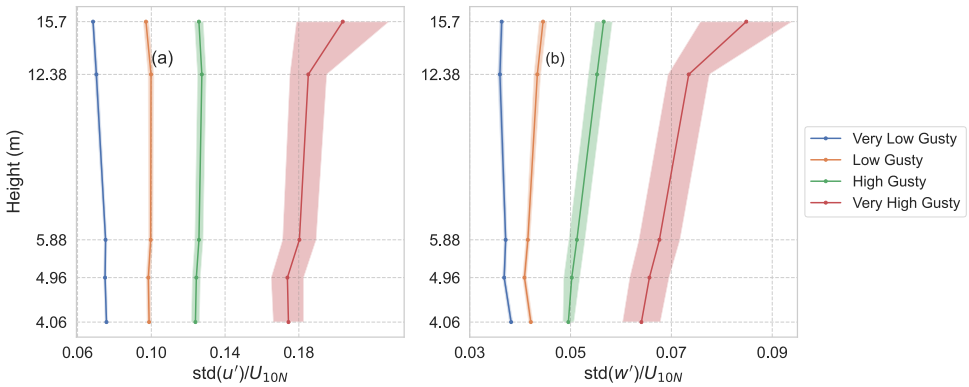

Fig. 5 Vertical structure of the normalized wind turbulences. a The profiles of $std(u')/U_{10N}$. **b** The profiles of $std(w')/U_{10N}$. The colors represent different levels of gustiness as shown in Fig. 4 and the shaded areas show the standard errors of the means.

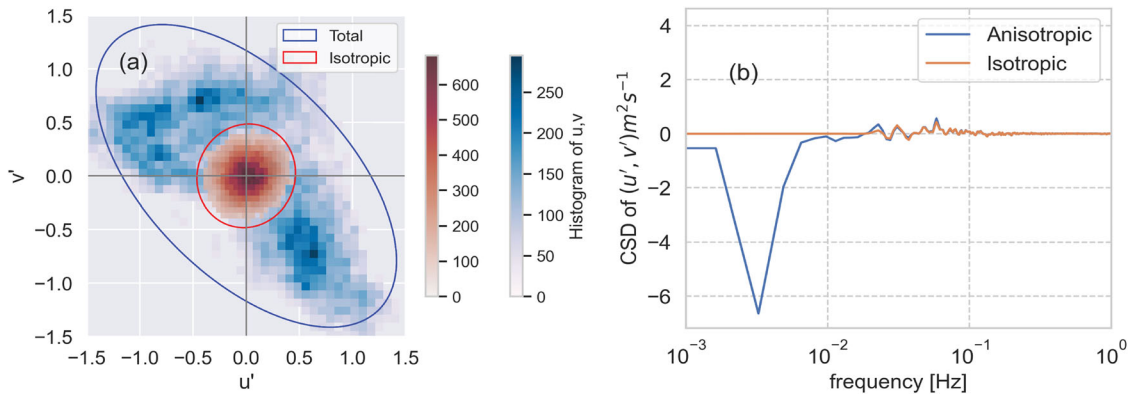

Fig. 6 Anisotropic properties of wind turbulence in one gusty run. a 2-D histogram of the wind turbulence (u',v'). The color represents the counts within each bin. Blue is raw data; red is after one minute high passed filtering. Within 30 min (1 run), there are 90,000 points in each subplot. The red and blue ellipses mark the confidence intervals of (u',v'), 95% of points are located within the oval. **b** Cospectrum of u' and v'.

turbulence intensity, the transfer rate of the momentum flux is regarded as consistent.

In Fig. 6a, we present heat maps representing the turbulence distributions for a selected gusty run. The wind speed in this run is 4.7 ms^{-1}, and G_0 is 0.214. By applying a one-minute high-pass filter, we restore anisotropic turbulence to normal isotropic turbulence. The ellipses in the plot indicate the 95% confidence intervals of the distributions. The anisotropic properties of horizontal velocity distribution are predominantly influenced by low-frequency motion, consistent with previous studies[31,32]. This is demonstrated further in Fig. 6b, which displays the cospectrum of u' and v' for this run. The cospectrum confirms that the anisotropic properties arise primarily from low-frequency motion. It is important to note that in other runs, the cospectra may exhibit different magnitudes or shapes, but the anisotropy is primarily observed in the low-frequency domain.

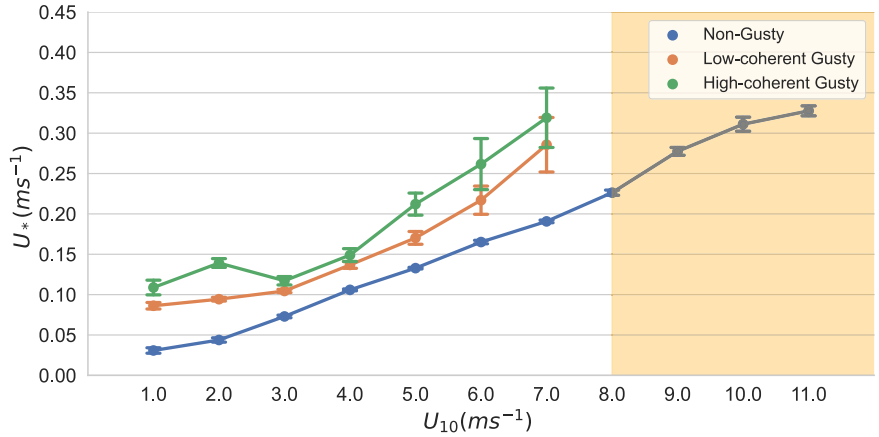

Fig. 7 Friction velocity vs wind speed under different gusty conditions. Non-gusty: $G_0 < 50$th percentile (blue); Low-coherent gusty: $G_0 > 50$th percentile & $cov(u',v') < 0.04$ (orange); high-coherent gusty: $G_0 > 50$th percentile & $cov(u',v') < 0.04$ (green). The error bars denote the standard errors of the means. U_{10} is calculated by the COARE 3.5 algorithm using atmosphere bulk parameters measured on *FLIP*. Yellow shaded area marks the data from the cold front event.

To further explore the influence of turbulence anisotropy on the momentum flux, we calculated $cov(u',v')$ for each of the gusty runs (i.e., $G_0 > 0.165$). Next, we classified them using the 50th percentile as either high-coherent gusty ($cov(u'v') > 0.04$ & $G_0 > 0.165$), or low-coherent gusty ($cov(u'v') \le 0.04$ & $G_0 > 0.165$). We then plot U_* vs U_{10N} in Fig. 7 to show the covariance effect on the momentum flux. Note that for wind speeds above 8 ms^{-1}, all our data exhibit $G_0 < 0.165$, leading to their classification as non-gusty. Between 2–4 ms^{-1}, higher coherence in the gusty spectrum leads to higher U_* for the same U_{10N} as compared to non-gusty conditions. Beyond 4 ms^{-1}, the trend persists but is not statistically significant. Comparing non-gusty to gusty, we observed a consistent trend in U_{10N} vs U_* with a statistically significant offset. Under gusty conditions, the momentum flux can be enhanced, and this amplification can be further reinforced by the high coherence properties of the wind. For wind speed over 8 ms^{-1} (shaded area in Fig. 7), this trend may still exist, but the platform did not collect any speed gusty events. This finding indicates that accurate parameterization of the momentum flux must consider gustiness as a contributing factor. Here, we should note that we think it is gustiness that causes vertical mixing even though precipitation/cloudiness can nearly simultaneously increase vertical mixing and gustiness. It is because for other common gustiness sources, such as heterogeneity of wind field or atmospheric stability, gustiness tends to be more pronounced. This makes gustiness usually regarded as an independent factor for flux parameterization[1,11,17,33] instead of vertical mixing.

DISCUSSION

Gusty wind can be decomposed into its isotropic and anisotropic portions, shown as Eq. (7), hence, the wind stress can also be decomposed into two terms[24,31,32,34],

$$\begin{aligned}(u',v',w') &= (u'_t,v'_t,w'_t) + (u'_g,v'_g,w'_g)\\ \tau_x &= -\rho\overline{u'w'} = -\rho(\overline{u_t w_t} + \overline{u_g w_g})\\ \tau_y &= -\rho\overline{v'w'} = -\rho(\overline{v_t w_t} + \overline{v_g w_g}),\end{aligned} \tag{7}$$

where u'_t, v'_t, and w'_t are isotropic wind turbulence components and u'_g, v'_g, and w'_g are the anisotropic wind components due to gustiness. The cross terms, $\overline{u_t * w_g}$ and $\overline{u_g * w_t}$, are negligible and are neglected[32]. Therefore, (u'_t,v'_t,w'_t) is the high-frequency (period <1 min) isotropic turbulence, and (u_g,v_g,w_g) is the lower-frequency (period ≥min) anisotropic turbulence. The decomposition relies on the low-frequency band to capture the impact of gustiness. Following Eq. (7), we finally decompose the flux into turbulent (isotropic) momentum flux and anisotropic momentum flux due to gustiness:

$$\begin{aligned}U_{*aniso} &= \left[\left(-\overline{u'_g w'_g}\right)^2 + \left(-\overline{v'_g w'_g}\right)^2\right]^{1/4}\\ U_{*iso} &= \left[\left(-\overline{u'_t w'_t}\right)^2 + \left(-\overline{v'_t w'_t}\right)^2\right]^{1/4}.\end{aligned} \tag{8}$$

The anisotropic flux mainly originates from the low-frequency band, as it is the frequency range where the anisotropic properties originate. Figure 8 shows the variation of these two types of momentum flux during the passage of a cold front, which caused high gustiness during CASPER from Oct-18 to Oct-20. The figure is broken into three sections (i), (ii), and (iii) which correspond to those in Fig. 3 and predominantly represent a non-gusty period, a gusty period before the cold front, and a non-gusty period when the cold front arrives, respectively. The green points represent the ratio of U_{*aniso} to U_{*iso}. When the wind is gusty, U_{*aniso}/U_{*iso} is typically above one, which means the anisotropic momentum flux is higher than the isotropic momentum flux. This reached a peak on Oct-18 when, U_{*aniso} was 30% higher than U_{*iso}. In contrast, under non-gusty conditions, $U_{*aniso}/U_{*iso} < 1$. Indeed, a higher anisotropic U_* component can potentially lead to a stronger coupling between swell and gustiness, as demonstrated in[28]. This strengthened coupling process can, in turn, result in enhanced vertical mixing within the air-sea boundary layer.

Figure 9a displays the vertical profiles of the anisotropic flux. To eliminate the influence of wind speed, the values are normalized by U_{10N}, which is calculated from the wind speed recorded at 12.38 m. The figure illustrates that the isotropic momentum flux (green profile) remains constant with height, regardless of gustiness. The anisotropic flux under non-gusty conditions (blue profile) also exhibits a constant profile. However, under gusty conditions, the anisotropic momentum flux (red profile) displays a vertical gradient, with the normalized U_* increasing with height. This suggests that additional momentum is generated as a result of the anisotropic properties, specifically the fluctuations in the low-frequency wind flow. Additionally, U_* increases with height indicating that, under gusty conditions, the additional momentum originates from aloft and is subsequently transferred towards the sea surface. Once it reaches the surface, the momentum dissipates rapidly through frictional processes. Moreover, a proportional relationship between gustiness and sea surface roughness has been observed, indicating a strengthening of the air-sea surface coupling[28]. This increased mixing can also help to explain the decreased vertical shear of the wind speed across the entire layer

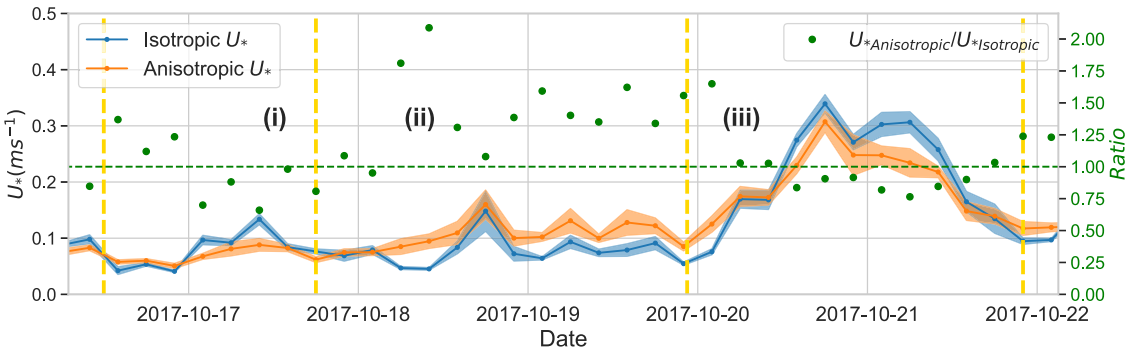

Fig. 8 Isotropic (blue) and anisotropic (orange) momentum flux time series along with gustiness (black). The yellow lines mark the three different gusty periods: (i) non-gusty period, (ii) gusty period, (iii) non-gusty period. The green points are the ratios of $U_{*anisotropic}$ and $U_{*isotropic}$. The green dashed line shows Ratio = 1.

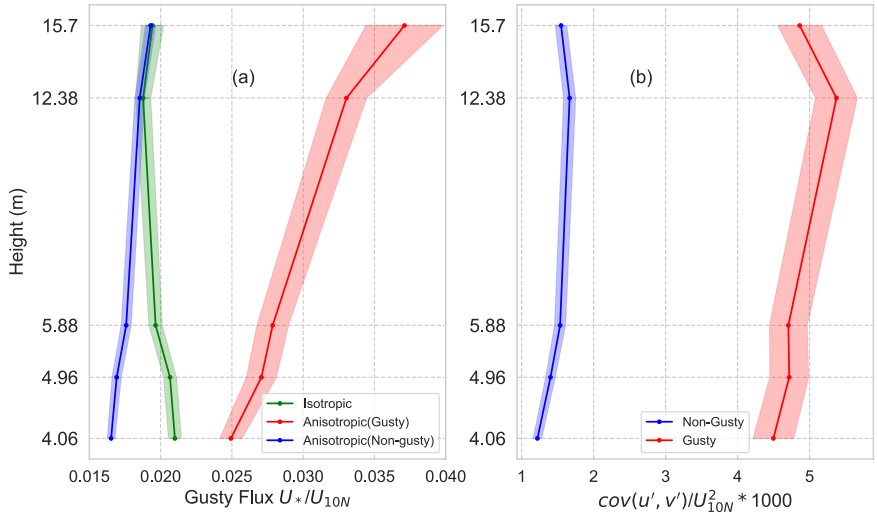

Fig. 9 Vertical profiles of decomposed momentum flux. a Isotropic (green) and anisotropic flux under gusty (red) and non-gusty (blue) conditions normalized by U_{10N} profiles. X-axis is the normalized flux. **b** Observed U_* profiles under different gusty conditions. U_* is normalized by the U_{*COARE}, calculated through COARE algorithm using the data collected at 12.38 m which is nearest to 10 m. Error bars denote the standard errors of the means.

shown in Fig. 4. Based on this finding, we can infer that the dissipation of wind energy at the sea surface is enhanced. This strengthened vertical mixing is likely associated with changes in wind speed profiles and the higher observed surface roughness.

In Fig. 9b, we plot mean vertical profiles of U_* normailzed by U_* predicted by COARE[35]. Results show that during very low and low gustiness, the friction velocity is underrepresented by COARE, but during high and very high gustiness, friction velocity is greater than predicted by COARE, i.e., $U_*/U_*^{COARE}>1$. Furthermore, there is evidence that friction velocity normalized this way has a vertical gradient during more gusty conditions. This indicates that during gusty conditions the assumption of a constant flux is no longer valid, and the momentum flux varies with height.

Figure 10 illustrates the variation in vertical mixing during gusty periods through the normalized power spectrum of w'. The vertical component of the wind collected by the IRGASON at 12.38 m is used, which well represents results at other heights. Each spectrum is the average under its respective level of gustiness, indicated by color. As gustiness increases, the peak frequency of w' shifts to higher values, accompanied by an increase in energy. For example, the mean spectral peak for the lowest gustiness bin ($0.08 < G_0 < 0.14$) is approximately 0.2, which shifts above 0.25 for the middle gustiness bin ($0.014 < G_0 < 0.018$), and over 0.3 for the highest bin ($G_0 > 0.18$). These findings suggest that gusts introduce additional turbulence into the boundary layer, thereby enhancing vertical mixing within the layer. Figure 11 further explores this idea by showing the w' wavelet power spectrum during the passage of the cold front. The w' is normalized by its standard deviation. In period (ii) of Fig. 8, two highly gusty periods, labeled as A and B, are observed. In Fig. 11, it demonstrates a significant increase in w' during high gustiness periods (A and B), indicating a greater transfer of energy into gusty frequency turbulence from the underlying basic flow. As a result, the anisotropic turbulence associated with gustiness leads to an amplification in energy within the vertical component of the wind. This, in turn, enhances the momentum flux. The heightened w' values during high gustiness periods signify the intensified vertical motion and the increased contribution of the vertical component to the overall momentum transfer.

We have established that the momentum flux is increased with higher gustiness because of the strengthened vertical mixing. Here, we put forward a possible explanation. Gusts manifest changes in wind direction or wind speed which generate a centrifugal force or acceleration force, respectively. This extra force must be balanced by the slope of the momentum flux (Eq. (9)),

$$F_{centrifugal} + F_{acceleration} = -\rho\frac{\partial u_*}{\partial z}, \tag{9}$$

which, according to similarity theory[8], equals zero. This means that gustiness can change the vertical structure of the marine

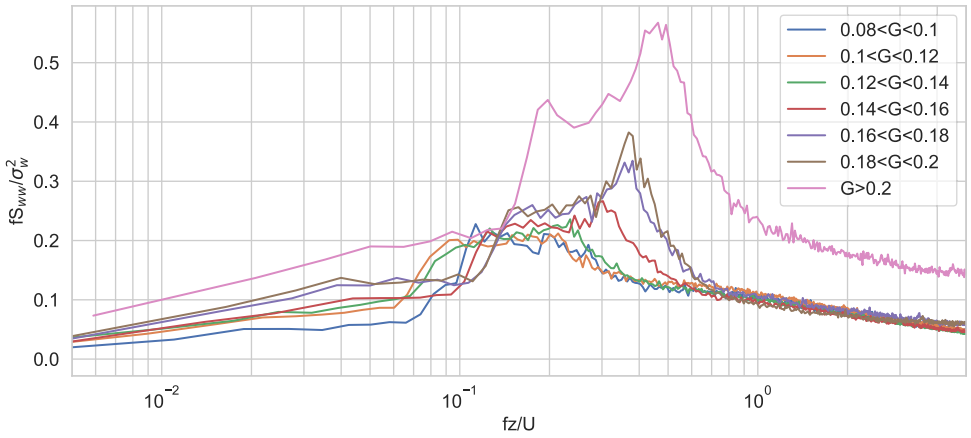

Fig. 10 Normalized power spectrum of the vertical component of wind speed under different gusty conditions. The y-axis is the wave spectrum normalized by the variance of w', the x-axis is the normalized frequency. The color denotes the level of gustiness following Eq. (5).

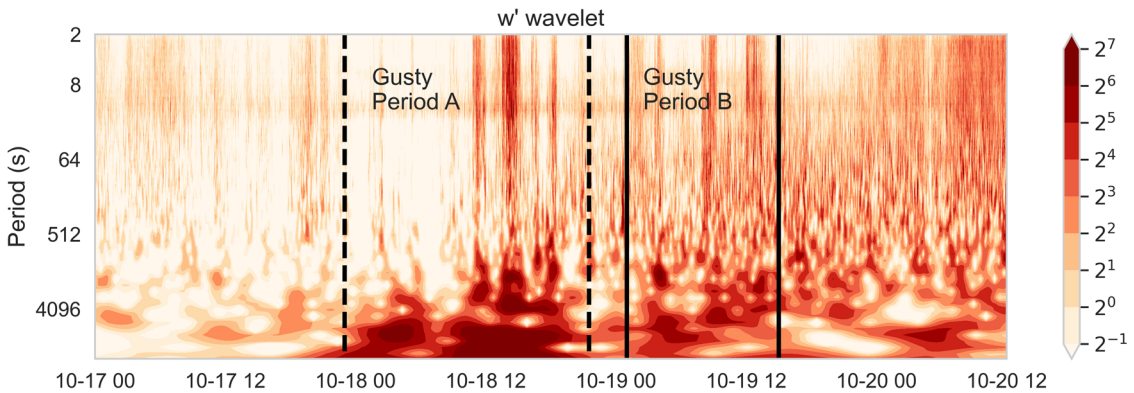

Fig. 11 Wavelet power spectrum of the vertical component of wind speed during the passage of the cold front. Results shown in w' wavelet power spectrum have already passed the significance test. Gusty period A & B are gusty events in period (ii) shown in Fig. 8.

atmospheric surface layer because the slope is no longer zero. This process can be further demonstrated using mixed length theory[36], which shows that the product of horizontal and vertical fluctuations can be calculated by

$$\overline{u'w'} = K_m \frac{\partial \overline{u}}{\partial z}, \tag{10}$$

where,

$$K_m = L^2 \left| \frac{\partial \overline{w}}{\partial z} \right|. \tag{11}$$

L is the mixed length and K_m is the eddy viscosity. Normally, we can use w' to approximately evaluate the magnitude of $L\frac{\partial \overline{w}}{\partial z}$ [37],

$$L \frac{\partial \overline{w}}{\partial z} \sim \frac{\partial w'}{\partial z}. \tag{12}$$

Hence, we know that the vertical mixing within the air-sea boundary layer is related to the mixed length, which further affects the eddy viscosity in the marine atmospheric surface layer. Therefore, we suggest the effect of gustiness on the momentum flux can be attributed to the changes in eddy viscosity, which enhances the exchange of momentum between the atmosphere and ocean surface and alters the constant flux layer.

Our findings show that, when it is gusty, the flux layer is not consistent with the widely adopted theory put forward by Monin and Obukhov[8]. When U_* is not constant with height, we cannot use the measurement at one height to represent the whole layer. This is impactful for observational studies because it means measurements at multiple heights are necessary to accurately estimate the vertical variability of the momentum flux and to quantify the total flux under gusty conditions. Another study, using the same dataset, revealed that similarity theory is more prone to failure than previously assumed, despite its general acceptance in numerous scenarios[10]. Through our study, it indicates that gusty conditions may significantly influence the applicability of MOST theory. Furthermore, because the boundary layer does not adhere to Monin–Obukhov Similarity Theory under gusty conditions, it is not possible to accurately convert to 10 m neutral conditions as is the common protocol. This means inherent uncertainty exists when comparing flux measurements made at different heights or gustiness regimes. These findings are also of critical importance for wind stress parameterization schemes which use U_{10N} to predict the momentum flux under the constant flux layer assumption. During gusty conditions, when the assumption of constant flux in the flux layer theory does not hold, simulations of wind-driven processes such as currents, waves, and weather becomes inaccurate. This emphasizes the importance of accounting for the influences of gustiness on parameterization schemes, particularly in the context of extreme event forecasting where gustiness can be high. Therefore, it becomes crucial to develop a better understanding of the flux layer to ensure accurate wind stress parameterizations. By accounting for gustiness and incorporating its effects into parameterization schemes, more reliable and precise predictions can be achieved for various wind-driven processes and extreme events.

Overall, this study highlights the important influences of gustiness on momentum flux which is largely underexplored and much needed to improve parameterizations. In this study, using a vertical array of high-frequency wind measurements collected from the stable R/P FLIP, we found that gustiness can promote vertical mixing which diminished the vertical gradient of wind speed. We also found that gusty conditions are correlated with significant anisotropic wind turbulence. When the momentum flux is decomposed into its isotropic and anisotropic components, the isotropic momentum flux mainly follows the wind speed tendency. Under gusty conditions, the contribution from the anisotropic flux to the total flux can be greater than the contribution from the isotropic flux. Additionally, more energy in w' is coming from the cascading turbulence originating from low frequency wind, and the eddy viscosity is found to be increased under gusty conditions. The strengthened w' then covaried with wind horizontal components which further increases the momentum flux.

We believe the increased mixing due to gustiness is important for refining air-sea momentum flux parameterization, since the prevailing constant flux layer model does not consider the effects of gustiness. In regions characterized by enhanced turbulence, such as frontal areas, the importance of gustiness in weather and climate prediction cannot be understated. We suggest incorporating the turbulence intensity (gustiness) into existing parameterizations, given its clear impacts on eddy viscosity in the air-sea boundary layer. Furthermore, our exploration of gustiness suggests a potential need to build a novel theoretical boundary layer model. The constant flux layer theory assumes that the air-sea boundary is a "solid" or "fixed" boundary, which cannot be moved or resonant. However, the ocean has a free surface which varies with the atmosphere. It has been already observed that gustiness can cause a rougher ocean surface which further fosters the evolution of surface gravity waves[28]. The vertical mixing related to gustiness likely plays a key role in this phenomenon. Ultimately, gustiness should receive more attention in air sea coupling given its indispensable significance in the parameterization of the momentum flux.

METHODS

CASPER instruments and gusty conditions

During CAPSER, the platform's motion is considered to have a negligible impact on wind flux measurements[38]. Figure 1b shows the location of the platform during CASPER. *FLIP* was equipped with a 13-m mast on its port boom outfitted with a vertical array of ultrasonic anemometer-thermometers and open-path gas analyzers: five Campbell Scientific IRGASONs (integrated gas analyzer and sonic anemometer), one combined Campbell Scientific CSAT-3, LiCOR 7500A. The IRGASONs collected concurrent 3-D high-frequency (50 Hz) wind vectors (u,v,w), air temperature, and humidity at six heights between 4 and 16 m above the mean water level. IRGASON can provide highly reliable wind measurements which has been widely used in many previous studies[15,17,39]. The errors of u and v are less than 8 cm s^{-1}, and the error of w is less than 4 cm s^{-1}. More details about instruments and how the wind measurements were made can be found in the technical report. In this study, due to data quality concerns, the IRGASON mounted at 8.9 m was not used. A more complete description of the CASPER experiment, instruments, and data can be found in the papers mentioned.

In data processing, we removed all wind data that were distorted by *FLIP*'s superstructure, leaving only data when the sensors were facing the winds (Fig. 2a). To calculate the flux u, v, and w were divided into bins of 30 min. Within each bin, we deleted (interpolated through) any data greater than five standard deviations of the mean. Next, we determined the mean wind speed, the fluctuations (u',v',w'), and U_*. Subsequently, using the COARE algorithm[11], we derived U_{10N} from data measured at 12.38 m, given its proximity to 10 m. Finally, for every bin at each measurement height, we quantified the gustiness using Eq. (6). For each measurement height we calculated the cumulative distribution function of gustiness (Fig. 2b). Next, following Lyu et al. [28], we classified the data into four gustiness regimes based on the 25th, 50th, and 75th percentiles. Overall, this is the methodology we used to define gustiness (Fig. 2b).

DATA AVAILABILITY

The data used in this article can be accessed at https://doi.org/10.18738/T8/OCBIST. The data and code files are saved in Matlab format and do not require registration to be accessed.

Received: 18 July 2023; Accepted: 18 January 2024;
Published online: 06 February 2024

REFERENCES

1. Webster, P. J. & Lukas, R. TOGA COARE: The coupled ocean–atmosphere response experiment. *Bull. Am. Meteorol. Soc.* **73**, 1377–1416 (1992).
2. Collins, C. O., Potter, H., Lund, B., Tamura, H. & Graber, H. C. Directional wave spectra observed during intense tropical cyclones. *J. Geophys. Res. Oceans* **123**, 773–793 (2018).
3. Kara, B., Metzger, E. J. & Bourassa, M. A. Ocean current and wave effects on wind stress drag coefficient over the global ocean. *Geophys. Res. Lett.* **34**, L01604 (2007).
4. Potter, H. The cold wake of typhoon Chaba (2010). *Deep Sea Res. Part I Oceanogr. Res. Pap.* **140**, 136–141 (2018).
5. Moum, J. & Smyth, W. Upper ocean mixing processes. *Encycl. Ocean Sci.* **6**, 3093–3100 (2001).
6. Potter, H., Drennan, W. M. & Graber, H. C. Upper ocean cooling and air-sea fluxes under typhoons: A case study. *J. Geophys. Res. Oceans* **122**, 7237–7252 (2017).
7. Zavarsky, A. et al. The influence of air-sea fluxes on atmospheric aerosols during the summer monsoon over the tropical Indian Ocean. *Geophys. Res. Lett.* **45**, 418–426 (2018).
8. Monin, A. S. & Obukhov, A. M. Basic laws of turbulent mixing in the surface layer of the atmosphere. *Contrib. Geophys. Inst. Acad. Sci. USSR* **151**, e187 (1954).
9. Mahrt, L., Miller, S., Hristov, T. & Edson, J. On estimating the surface wind stress over the sea. *J. Phys. Oceanogr.* **48**, 1533–1541 (2018).
10. Ortiz-Suslow, D. G., Kalogiros, J., Yamaguchi, R. & Wang, Q. An evaluation of the constant flux layer in the atmospheric flow above the wavy air-sea interface. *J. Geophys. Res. Atmos.* **126**, e2020JD032834 (2021).
11. Fairall, C. W., Bradley, E. F., Hare, J., Grachev, A. A. & Edson, J. B. Bulk parameterization of air–sea fluxes: Updates and verification for the COARE algorithm. *J. Clim.* **16**, 571–591 (2003).
12. Stewart, R. The air-sea momentum exchange. *Bound. Lay. Meteorol.* **6**, 151–167 (1974).
13. Large, W. & Pond, S. Open ocean momentum flux measurements in moderate to strong winds. *J. Phys. Oceanogr.* **11**, 324–336 (1981).
14. Vincent, C. L., Graber, H. C. & Collins, C. O. III Effect of Swell on Wind Stress for Light. *Moderat. Winds J. Atmos. Sci.* **77**, 3759–3768 (2020).
15. Tamura, H., Drennan, W. M., Collins, C. O. & Graber, H. C. Turbulent airflow and wave-induced stress over the ocean. *Bound. -Lay. Meteorol.* **169**, 47–66 (2018).
16. Potter, H. Swell and the drag coefficient. *Ocean Dyn.* **65**, 375–384 (2015).
17. Potter, H., Collins, C. O. & Ortiz-Suslow, D. G. Pier-Based Measurements of Air-Sea Momentum Fluxes Over Shoaling Waves During DUNEX. *J. Geophys. Res. Oceans* **127**, e2022JC018801 (2022).
18. Zeng, X., Zhang, Q., Johnson, D. & Tao, W. Parameterization of wind gustiness for the computation of ocean surface fluxes at different spatial scales. *Mon. Weather Rev.* **130**, 2125–2133 (2002).
19. Redelsperger, J.-L., Guichard, F. & Mondon, S. A parameterization of mesoscale enhancement of surface fluxes for large-scale models. *J. Clim.* **13**, 402–421 (2000).
20. Zeng, X., Zhao, M. & Dickinson, R. E. Intercomparison of bulk aerodynamic algorithms for the computation of sea surface fluxes using TOGA COARE and TAO data. *J. Clim.* **11**, 2628–2644 (1998).
21. Esbensen, S. K. & McPhaden, M. J. Enhancement of tropical ocean evaporation and sensible heat flux by atmospheric mesoscale systems. *J. Clim.* **9**, 2307–2325 (1996).

22. Williams, A. & Hacker, J. The composite shape and structure of coherent eddies in the convective boundary layer. *Bound. -Lay. Meteorol.* **61**, 213–245 (1992).
23. Harrop, B. E., Ma, P. L., Rasch, P. J., Neale, R. B. & Hannay, C. The role of convective gustiness in reducing seasonal precipitation biases in the Tropical West Pacific. *J. Adv. Model. Earth Syst.* **10**, 961–970 (2018).
24. Cheng, X., Wu, L., Hu, F. & Zeng, Q. C. Parameterizations of some important characteristics of turbulent fluctuations and gusty wind disturbances in the atmospheric boundary layer. *J. Geophys. Res. Atmos.* **117**, D08113 (2012).
25. Babanin, A. V. & Makin, V. K. Effects of wind trend and gustiness on the sea drag: Lake George study. *J. Geophys. Res. Oceans* **113**, C02015 (2008).
26. Lyu, M., Potter, H. & Collins, C. O. The impacts of gustiness on Air–Sea momentum flux. *Fluids* **6**, 336 (2021).
27. Jiang, Q., Wang, S. & Sullivan, P. Large-eddy simulation study of log laws in a neutral Ekman boundary layer. *J. Atmos. Sci.* **75**, 1873–1889 (2018).
28. Lyu, M., Potter, H., Collins, C. O., Yang, X. & Wang, X. The impacts of gustiness on the evolution of surface gravity waves. *Geophys. Res. Lett.* **50**, e2023GL104085 (2023).
29. Wang, Q. et al. CASPER: Coupled air–sea processes and electromagnetic ducting research. *Bull. Am. Meteorol. Soc.* **99**, 1449–1471 (2018).
30. Petersen, E. L., Mortensen, N. G., Landberg, L., Højstrup, J. & Frank, H. P. *Wind power meteorology. Part I: Climate and turbulence*. 1 (Wind Energy, 1998).
31. Zeng, Q., Cheng, X., Hu, F. & Peng, Z. Gustiness and coherent structure of strong winds and their role in dust emission and entrainment. *Adv. Atmos. Sci.* **27**, 1–13 (2010).
32. Cheng, X., Zeng, Q. C. & Hu, F. Characteristics of gusty wind disturbances and turbulent fluctuations in windy atmospheric boundary layer behind cold fronts. *J. Geophys. Res. Atmos.* **116**, D06101 (2011).
33. Bradley, E. & Weller, R. Fourth workshop of the TOGA COARE air–sea interaction (flux) working group, *University Corporation for Atmospheric Research Report, UCAR, Boulder, CO,* (1997).
34. Li, Q.-L., Cheng, X.-L. & Zeng, Q.-C. Gustiness and coherent structure under weak wind period in atmospheric boundary layer. *Atmos. Sci. Lett.* **9**, 52–59 (2016).
35. Edson, J. B. et al. On the exchange of momentum over the open ocean. *J. Phys. Oceanogr.* **43**, 1589–1610 (2013).
36. Bradshaw, P. Possible origin of Prandt's mixing-length theory. *Nature* **249**, 135–136 (1974).
37. Holton, J. R. An introduction to dynamic meteorology. *Am. J. Phys.* **41**, 752–754 (1973).
38. Ortiz-Suslow, D. G., Wang, Q., Kalogiros, J. & Yamaguchi, R. A method for identifying Kolmogorov's inertial subrange in the velocity variance spectrum. *J. Atmos. Ocean. Technol.* **37**, 85–102 (2020).
39. Drennan, W. M., Kahma, K. K. & Donelan, M. A. On momentum flux and velocity spectra over waves. *Bound. Lay. Meteorol.* **92**, 489–515 (1999).

ACKNOWLEDGEMENTS

I would like to express our gratitude to the Office of Naval Research (ONR) for funding the CAPSPER campaign through Grant N0001418WX01087, and to all those who were involved in the project.

AUTHOR CONTRIBUTIONS

Meng Lyu, Henry Potter conceived the idea. David G. Ortiz-Suslow and Qing Wang collected and provided the data for analysis. Xiaoqi Wang and Meng Lyu worked together for data analysis and conclusions, also preparing the main manuscript. Henry Potter and David G. Ortiz-Suslow helped with further revisions of the manuscript.

COMPETING INTERESTS

The authors declare no competing interests.

ETHICS APPROVAL AND CONSENT TO PARTICIPATE

All subjects gave their informed consent for inclusion before they participated in this study. The study was conducted in the accordance with the requirements with the protocols requited by Nature Portfolio.

ADDITIONAL INFORMATION

Correspondence and requests for materials should be addressed to Meng Lyu or Xiaoqi Wang.